PHYSICAL REVIEW B **111**, 024308 (2025)

Influence of H_2S on carbon aggregation processes under high temperature and pressure conditions

D. Murayama,[1,*] S. Ohmura,[2] R. Kodama,[1,3] and N. Ozaki[1,3]
[1]*Graduate School of Engineering, Osaka University, Osaka 565–0871, Japan*
[2]*Faculty of Engineering, Hiroshima Institute of Technology, Hiroshima 731–5193, Japan*
[3]*Institute of Laser Engineering, Osaka University, Osaka 565–0871, Japan*

(Received 7 August 2024; revised 27 November 2024; accepted 9 December 2024; published 21 January 2025)

We performed *ab initio* molecular dynamics simulations for CH_4-H_2S mixtures at temperatures ranging from 3000 to 10 000 K and pressures up to 1500 GPa. We calculated pair distribution functions and bond-overlap populations to examine the structural and chemical bonding properties of this mixed system. The results indicate the breaking of C–H and S–H bonds, followed by the formation of strong covalent C–C and C–S bonds, suggesting phase separation between hydrogen and heavier atoms such as carbon and sulfur. Moreover, our findings reveal that hydrogen sulfide promotes the molecular dissociation of methane and facilitates carbon aggregation below ~200 GPa at 4000 K. However, above this pressure, it potentially inhibits carbon aggregation because of the strong correlation between carbon and sulfur atoms. Our insights into the microscopic behavior of this mixture can potentially enhance the understanding of diamond formation processes within the icy giants Uranus and Neptune.

DOI: 10.1103/PhysRevB.111.024308

I. INTRODUCTION

Hydrocarbons can be observed in various settings, including inertial confinement fusion capsules [1], material synthesis experiments [2], and planetary interiors [3]. Methane (CH_4) is an abundant hydrocarbon within the mantles of the icy giants Uranus and Neptune, where temperatures and pressures range from 2000 K and 20 GPa to 8000 K and 600 GPa, respectively [4,5]. Therefore, understanding the equation of state (EOS), structural properties, chemical bonding properties, and kinetics of CH_4 under these extreme conditions is crucial for elucidating the interior structure and thermal evolution of the icy giants. In addition, with the discovery of numerous Neptune-class exoplanets [6–8] beyond our solar system, research on dense hydrocarbon systems under a wide range of thermodynamic conditions has gained considerable interest.

Structural transformations from hydrocarbons to diamonds under high temperatures and pressures [9–22] have significant implications for the icy giants. For example, diamond precipitation serves as a heat source within these planets [2], and understanding the fundamental processes of diamond formation from CH_4 can help elucidate their thermal evolution. Several studies have shown that diamond forms through a liquid–liquid phase separation of metallic hydrogen and carbon [19], following the molecular dissociation and polymerization of hydrocarbons [23–28]. These transformations occur over timescales ranging from subnanoseconds [2,14,19,29] to tens of microseconds [21], depending on the temperature and pressure conditions. Computational simulations of C/H systems containing over 10 000 atoms, using machine learning potentials trained on *ab initio* molecular dynamics (AIMD) data, have demonstrated that the liquid–liquid phase separation and diamond formation can occur at temperatures below 3000–3500 K and pressures above 200 GPa, irrespective of the carbon concentration [18]. These findings can help explain the low luminosity of Uranus.

Several carbon-bearing mixture systems, including CH_4-H_2 compounds [30–32], CH_4-He compounds [33], C–H–O ternary systems [2,34–37], and C–H–N–O quaternary systems [24,38–44], have been previously investigated. A static compression experiment with diamond-anvil cell by Kadobayashi *et al.* revealed that water promotes the molecular dissociation of CH_4 under extreme conditions because of the solvent effect of ionized water [36]. Consequently, diamond formation in these mixtures can occur at lower temperatures than in the CH_4 systems [10,11]. Using AIMD simulations, Lee *et al.* demonstrated that ionized water induces the ionization of CH_4, rendering the mixture electronically conductive [34]. These findings indicate that diamond formation processes are strongly influenced by the addition of materials and elements under extreme conditions relevant to the icy giants. Therefore, elucidating the behavior of hydrocarbons and complex mixtures under such conditions is critical for advancing our understanding of the planetary interiors and thermal evolution.

Hydrogen sulfide (H_2S) has attracted significant interest for its ability to transition to a superconductive state under high pressures [45]. Moreover, H_2S is considered an analogous hydride with hydrogen bonds similar to those in H_2O [46,47] because sulfur and oxygen belong to the same family in the periodic table. Sulfur is the tenth most abundant element in the solar system [48] and is particularly relevant for exploring whether H_2S has the same effect on hydrocarbons as water. Atmospheric observations have shown that H_2S exists above

---

[*] Contact author: murayamad@ef.eie.eng.osaka-u.ac.jp

the cloud decks of the icy giants [49]. Motivated by these findings, we focused on H_2S and investigated its effects on carbon aggregation processes in a mixture of CH_4 and H_2S.

In this paper, we describe behaviors of CH_4-H_2S mixture systems at temperatures ranging from 3000 to 10 000 K and pressures up to 1500 GPa using AIMD simulations. We examined the structural and chemical bonding properties of C–C and C–S bonds within this mixed system and employed Mulliken population analysis [50,51] to characterize the chemical bonding properties. Furthermore, we assessed the carbon diffusivities and bond lifetimes of C–C bonds to understand the kinetics of carbon aggregation in this mixed system.

II. COMPUTATIONAL METHODS

We employed AIMD simulations for two types of systems: the CH_4-H_2S mixture and CH_4, to examine the influence of H_2S on carbon aggregation processes. We calculated 82 distinct thermodynamic conditions (ranging up to 10 000 K and 1500 GPa), with densities spanning from 2.0 to 7.0 g/cm^3 for the mixed system and from 1.2 to 4.5 g/cm^3 for the CH_4 system. The resulting EOS data are summarized in Tables SI and SII of the Supplemental Material [52]. All AIMD simulations were conducted using the QXMD code [53,54], where atomic forces were derived from electronic states calculated using the projector augmented-wave method [55,56] within the density-functional theory framework [57–59]. The electronic states were populated according to the Fermi-Dirac distribution, with the electronic temperature set equal to that of the ions. For the electronic exchange-correlation functional, the generalized gradient approximation in the Perdew-Burke-Ernzerhof parametrization [60] was employed.

A. CH_4-H_2S mixture system

For the mixed system, the cutoff energies for the plane waves were 50 and 300 Ry for the electronic pseudo-wave functions and pseudo-charge density, respectively. As shown in Fig. S1 [52], the structural properties at 3.0 g/cm^3 and 4000 K converged well for the cutoff energy of 70 Ry. Moreover, the pressure and potential energy converged to values better than 1.0% and 0.5 mRy per atom, respectively, at 50 Ry compared to 150 Ry. Therefore, we concluded that convergence was achieved at 50 Ry. The energy density functional was minimized using an iterative scheme [53,61]. For Brillouin-zone sampling, only the Γ point was used, and with this k point, the static pressure at 3.0 g/cm^3 and 4000 K converged within 1.0% compared to the Monkhorst-Pack [62] $3 \times 3 \times 3$ grid. For the calculations, the 1s orbitals of hydrogen (with a cutoff radius of 1.1 bohr), the 2s and 2p orbitals of carbon (with cutoff radii of 1.3 and 1.5 bohr), and the 3s, 3p, and 3d orbitals of sulfur (with cutoff radii of 1.5, 1.5, and 2.0 bohr, respectively) were used as valence electrons.

For the molecular dynamics simulations, we used 32 CH_4 and 32 H_2S molecules for low-pressure conditions and 50 CH_4 and 50 H_2S for low temperature and high pressure conditions in a cubic supercell under periodic boundary conditions. To minimize convergence effects related to system size, we used the same number of CH_4 and H_2S molecules. For the initial configurations shown in Fig. S2 [52], we randomly arranged the molecules for each simulation to avoid bias toward certain molecular configurations. The physical properties were investigated using AIMD simulations in a canonical ensemble. The equations of motion were solved using the Nosé-Hoover thermostat technique [63,64] and an explicit reversible integrator [65], with a time step of 0.24 fs for all the thermodynamic conditions. The electronic temperature T_e was set equal to the ionic temperature. Each condition was run for 4.8–24.0 ps, depending on the temperature, to ensure accurate statistics for the quantities of interest.

B. CH_4 system

The CH_4 systems were also examined, and unless otherwise noted, the same scheme was used for the CH_4 systems as for the mixed systems. The cutoff energies for the plane waves were 50 and 300 Ry for the electronic pseudo-wave functions and pseudo-charge density, respectively. The pressure and potential energy converged to value better than 1.0% and 0.5 mRy per atom, respectively, at 50 Ry compared to 150 Ry. Therefore, we concluded that convergence was reached at 50 Ry and used this value as the cutoff energy. For Brillouin-zone sampling, only the Γ point was used. This choice of k point has been shown to produce good convergence for the EOS, as confirmed by a convergence test regarding k-point sampling [23].

For the molecular dynamics simulations, we used 64 CH_4 molecules for low pressure conditions and 100 CH_4 molecules for low temperature and high pressure conditions in a cubic supercell under periodic boundary conditions. Depending on the temperature conditions, each condition was run for 4.8–12.0 ps to obtain accurate statistics for the quantities of interest. However, we observed significant deviations of up to 4% in low pressure conditions compared to the results of Sherman *et al.* [23], which can be attributed to differences in cutoff energy, particle number, and simulation time employed.

III. RESULTS AND DISCUSSION

A. Pair distribution function

To gain insight into the structural properties of the CH_4-H_2S system, we examined the pair distribution functions over the temperature range of 4000 to 10 000 K. We focused particularly on 4000 K because this temperature yielded the most diverse results compared with the other temperatures. Figures 1(a)–1(f) show the pair distribution functions $g_{\alpha\beta}(r)$ for H–H, C–H, S–H, C–C, C–S, and S–S along the 4000 K isotherm, respectively. The $g_{\alpha\beta}(r)$ functions at the other temperatures are shown in Figs. S3–S6 [52].

As shown in Fig. 1(a), at 47 GPa the first peak in $g_{\mathrm{HH}}(r)$ emerges at approximately $r = 0.8$Å, indicating the formation of molecular hydrogen H_2 [23]. Furthermore, the first and second peaks merge as pressure increases, indicating the dissociation of the molecular hydrogen and an increase in the fraction of atomic hydrogen. The structural transition of hydrogen in the mixture resembles that observed in other hydrocarbon systems [18,20,23]. As shown in Figs. 1(b) and 1(c), at 47 GPa the first peaks in $g_{\mathrm{CH}}(r)$ and $g_{\mathrm{SH}}(r)$ appear at $r = 1.1$ and 1.4 Å, respectively, corresponding to the C–H bonds in CH_4 [23] and S–H bonds in H_2S [66]. These peaks

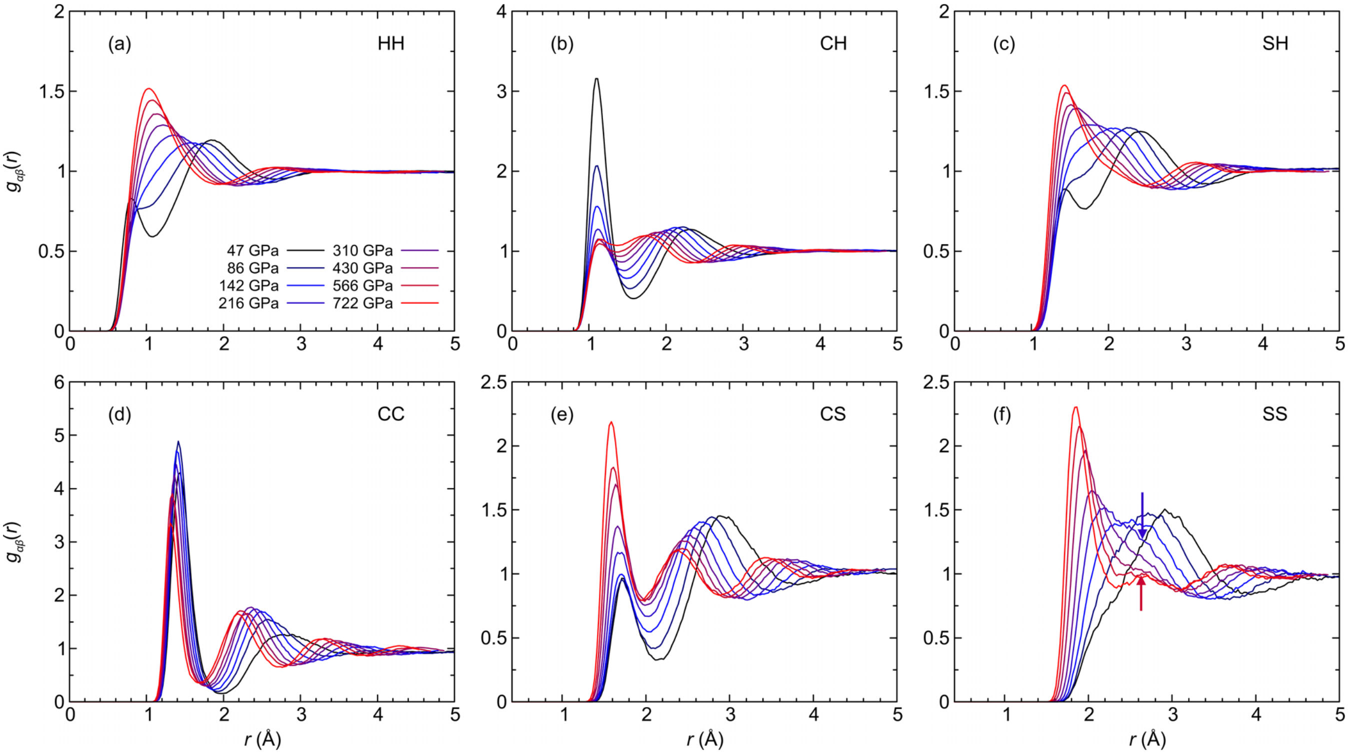

FIG. 1. Pair distribution functions at the temperature of 4000 K and pressures from 47 to 722 GPa for eight types of atom pairs: (a) H–H, (b) C–H, (c) S–H, (d) C–C, (e) C–S, and (f) S–S. The blue and red arrows in (f) indicate the hump and local peak, respectively.

broaden with increasing pressure because of the molecular dissociation of CH_4 and H_2S. Comparing the first peaks in $g_{\mathrm{CH}}(r)$ and $g_{\mathrm{SH}}(r)$, the hydrogen atoms are less correlated with sulfur atoms than with carbon atoms, suggesting that H_2S was less stable than CH_4.

As shown in Figs. 1(d) and 1(e), the first pronounced peaks in $g_{\mathrm{CC}}(r)$ and $g_{\mathrm{CS}}(r)$ appear at $r = 1.4$ and 1.7 Å, respectively, up to 722 GPa. Given the absence of C–C and C–S correlations in the initial atomic configuration, the appearance of these peaks suggests the formation of C–C and C–S bonds. The intensity of the first peak in $g_{\mathrm{CS}}(r)$ increases with increasing pressure, indicating a stronger correlation between carbon and sulfur atoms. From atomic configurations, chainlike carbon structures with C–S bonds were observed at 47 GPa (Fig. S11(a) [52]). When the pressure increases to 310 GPa, transient carbon complexes with varying coordination (up to fourfold) and several bonded sulfur atoms were formed (Fig. S11(c) [52]). As shown in Fig. 1(f), at 47 GPa no distinct first peak can be observed [67]; instead, a shoulder appears at approximately $r = 2.0$ Å, indicating that the S–S bonds were unstable. As the pressure increases, the intensity of the first peak in $g_{\mathrm{SS}}(r)$ increases, meaning a growing correlation in the interactions between sulfur atoms. Moreover, at pressures above ∼216 GPa, a hump appears at approximately 2.7 Å [Fig. 1(f), blue arrow] and transforms into a local peak at 566 GPa [Fig. 1(f), red arrow]. Notably, this phenomenon is not observed in pure sulfur systems [68] and the local peak is located at approximately $\sqrt{3}$ times the distance of the first peak in $g_{\mathrm{CS}}(r)$. Therefore, these signals indicate correlations between sulfur atoms bonded to the same carbon atoms. Such signals can also be observed under other temperature conditions, including up to 10 000 K, as shown in Fig. S6 [52]. This indicates that a strong correlation between carbon and sulfur atoms exists across an extensive range of thermodynamic conditions.

Based on the structural properties, C–C and C–S bonds, along with transient H_2, were formed after the molecular dissociation of CH_4 and H_2S. Because of the strong correlation between the C–C and C–S bonds, hydrogen atoms can be separated from the heavier atoms (C and S). The strong interactions between carbon and sulfur atoms influenced the structural properties of sulfur, resulting in the emergence of a local peak in $g_{\mathrm{SS}}(r)$.

B. Bond-overlap population

To elucidate the chemical bonding properties of the CH_4-H_2S system, we employed Mulliken population analysis [50,51], in which the electronic wave functions were expanded in an atomic orbital basis set (see the Supplemental Material [52] and Ref. [20]). Figures 2(a)–2(f) show time-averaged distributions of the bond-overlap population $[p_{\alpha\beta}(\bar{O})]$ along the 4000 K isotherm, providing a semiquantitative estimate of covalent-like bonding between α and β atomic types in H–H, C–H, S–H, C–C, C–S, and S–S pairs. The $p_{\alpha\beta}(\bar{O})$ results under the other temperature conditions are shown in Figs. S7–S10 [52]. We obtained $p_{\alpha\beta}(\bar{O})$ by creating a histogram of the partial bond-overlap population $O_{ij}(t)$ between ith and jth atoms, whose distances are within 10.0 bohr in all atomic configurations after equilibration. Notably, because the atomic orbital basis set used in the wave-function expansion is not unique owing to its incompleteness, a discussion of the absolute magnitudes of $\bar{O}$ would have little meaning. However, the trends in $\bar{O}$ remain unchanged for any

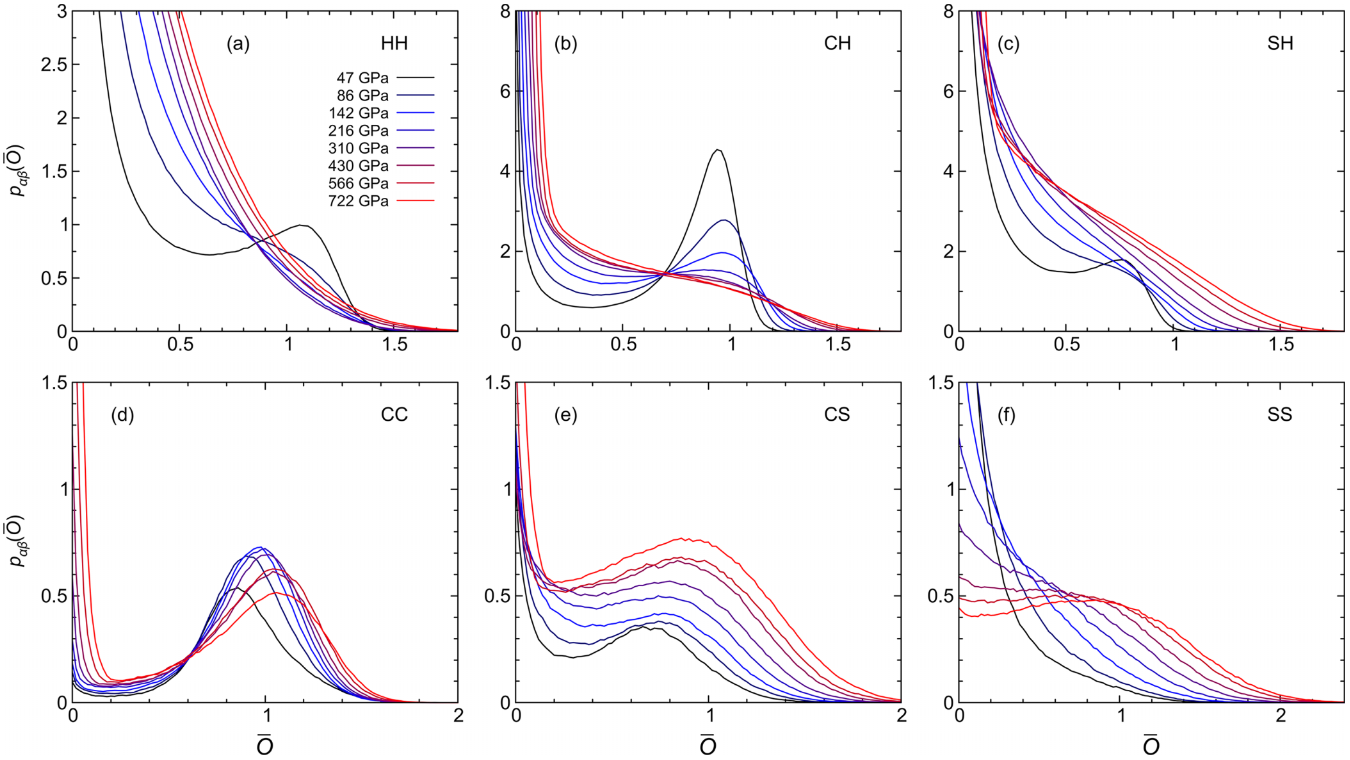

FIG. 2. Distributions $p_{\alpha\beta}(\bar{O})$ of the bond-overlap populations at the temperature of 4000 K and pressures from 47 to 722 GPa for eight types of atom pairs: (a) H–H, (b) C–H, (c) S–H, (d) C–C, (e) C–S, and (f) S–S.

choice of the atomic orbital basis set; therefore, a discussion of the relative changes in $\bar{O}$ is meaningful.

As shown in Figs. 2(a)–2(c), at 47 GPa, $p_{\mathrm{HH}}(\bar{O})$, $p_{\mathrm{CH}}(\bar{O})$, and $p_{\mathrm{SH}}(\bar{O})$ exhibit distinct peaks at approximately $\bar{O} = 1.1$, 1.0, and 0.8, respectively. The appearance of these peaks indicates the presence of covalent H–H, C–H, and S–H bonds. From the atomic configuration, as shown in Fig. S11(b) [52], molecular hydrogen and C–H and S–H bonds can be observed. The distinct peaks in $p_{\mathrm{HH}}(\bar{O})$ and $p_{\mathrm{SH}}(\bar{O})$ disappear with increasing pressure, meaning that the covalent interactions of H–H and S–H weakened, and molecular hydrogen and H_2S dissociated. The distinct peak in $p_{\mathrm{CH}}(\bar{O})$ persists up to 216 GPa and then shifts to a shoulder, indicating that the C–H bond retained its covalent nature even at 722 GPa.

As shown in Figs. 2(d) and 2(e), pronounced peaks in $p_{\mathrm{CC}}(\bar{O})$ and $p_{\mathrm{CS}}(\bar{O})$ at 47 GPa can be observed at approximately $\bar{O} = 0.8$ and 0.7, respectively, indicating the formation of covalent C–C and C–S bonds. As pressure increases, the peak in $p_{\mathrm{CC}}(\bar{O})$ shifts toward a larger $\bar{O}$ value and the peak in $p_{\mathrm{CS}}(\bar{O})$ intensifies, meaning the persistence of covalent C–C and C–S interactions at least up to 722 GPa. At 47 and 310 GPa, localized electron density between the carbon and sulfur atoms can be observed (Figs. S11(b) and S11(d) [52]). Additionally, we calculated the coordination number around C atoms to be 3.96 at 4000 K and 47 GPa. The almost four-coordination reflects the covalent-like interactions associated with the C atoms owing to sp^3 hybridization of the carbon atom. Figure 2(f) shows that the S–S bonds may exhibit covalent characteristics, given that $p_{\mathrm{SS}}(\bar{O})$ shows regions where $\bar{O} > 1.0$ under the three lowest pressure conditions. However, $p_{\mathrm{SS}}(\bar{O})$ does not exhibit a peak or shoulder. This indicates that the covalent interactions become weak. As pressure increases, the shape of $p_{\mathrm{SS}}(\bar{O})$ gradually transforms into a shoulder, eventually forming a shallow peak at 722 GPa, the highest pressure we examined. These chemical bonding properties suggest an increase in covalent interactions between sulfur atoms, reflecting a growing correlation between them, as shown in Fig. 1(f). Under these high pressure conditions, where C–C, C–S, and S–S exhibit strong covalent interactions, carbon and sulfur clusters may precipitate in the mixed system.

To examine the chemical bonding properties between carbon and sulfur in more detail, we investigated the time evolution of the partial bond-overlap population $O_{ij}(t)$ (see Ref. [20] for theoretical details). Figure 3(a) shows the time evolution of the partial bond-overlap populations between a selected carbon atom and its surrounding atoms at 4000 K and 310 GPa. $O_{\mathrm{C-S1}}(t)$ begins to increase at $t = 0.00$ ps, followed by more than ten oscillations, indicating the formation of a covalent C–S1 bond [see the atomic configuration in Fig. 3(b)]. At 0.17 ps, $O_{\mathrm{C-S1}}(t)$ decreases to zero, indicating the loss of the covalent nature of the C–S1 bond. From this perspective, the lifetime of the C–S1 covalent bond is estimated to be approximately 0.17 ps. An additional covalent bond can be observed between carbon and sulfur, the C–S2 bond, with a lifetime of approximately 0.15 ps. Therefore, multiple covalent bonds can form between carbon and sulfur under these conditions.

All temperatures investigated in this study are higher than the melting points of solid methane [10–13], where van der Waals interactions between molecules are dominant. Accordingly, the weak van der Waals interactions do not contribute to the chemical bonding properties and therefore have a negligible impact on the physical properties of the mixture, including the molecular dissociation of CH_4 and H_2S, atomic diffusivity, and carbon aggregation.

C. Diffusion coefficient

To investigate atomic diffusivities, we calculated the diffusion coefficients D_α for α = H, C, and S from the slopes of each mean-square displacement (MSD). To reduce errors owing to statistical noise, we divided the total trajectory over which the MSD was computed into shorter segments, as shown in Fig. S12 [52], and averaged the slopes of the MSDs from these time-divided segments to obtain D_α. Furthermore, we conducted a convergence test of the MSDs with respect to the system size at 4.0 g/cm^3 and 4000 K. Systems containing 64 and 100 molecules yield similar slopes (Fig. S13 [52]). The maximum uncertainties in D_H and D_C are within 2% (Table SIII [52]), while that in the D_S can reach 13%.

Figure 4(a) shows the diffusion coefficients of carbon and sulfur as functions of pressure along the 4000 K isotherm. Despite sulfur having a greater atomic mass than carbon, D_S exceeds D_C under most pressure conditions, which is attributed to the carbon aggregation. Both D_C and D_S decreased slightly with increasing pressure as particle interactions strengthened. Furthermore, D_C approaches D_S at higher pressures, which can be attributed to the increased correlation between the carbon and sulfur atoms, as discussed in Secs. III A and III B.

To compare the D_α values of the mixed and CH_4 systems, we calculated the deviation $(D_\alpha^{\mathrm{mixture}} - D_\alpha^{\mathrm{CH_4}})/D_\alpha^{\mathrm{CH_4}}$ for α = H and C, obtained using interpolation with modified Akima splines. The deviations in D_C are plotted in Fig. 4(b). The D_C value in the mixed system exhibits a significant positive deviation of up to 118% at approximately 540 GPa. This deviation suggests that the movement of carbon atoms was driven by strong correlations with the highly diffusive sulfur atoms, making the carbon atoms more diffusive.

As shown in Fig. 4(c), in the mixed system, D_H was more than four times larger than D_C and D_S for all pressures, reflecting the instability of CH_4 and H_2S along the 4000 K isotherm [9,24,26]. D_H exhibits a maximum at approximately 90 GPa, indicating the transition from a molecular fluid to an atomic fluid. As shown in Fig. 4(d), D_H shows notable deviations under low pressure conditions, which gradually decrease with increasing pressure. These deviations can be attributed to the molecular dissociation of H_2S and the enhanced molecular dissociation of CH_4 caused by the corrosive effect of H_2S.

D. Bond lifetime

Finally, we calculated the bond lifetimes τ_α for α = C–H, C–C, and C–S. To determine the lifetimes, we recorded the time it took for a formed bond to dissociate during AIMD simulations. The method for determining cutoff distances is detailed in Fig. S15 [52]. A convergence test of the bond lifetimes with respect to the system size and number of steps was performed at 4.0 g/cm^3 and 4000 K (310 GPa). The lifetime errors between the 64- and 100-molecule systems, with respect to system size and number of steps, were approximately within 2 and 0.4%, respectively (Fig. S16 [52]).

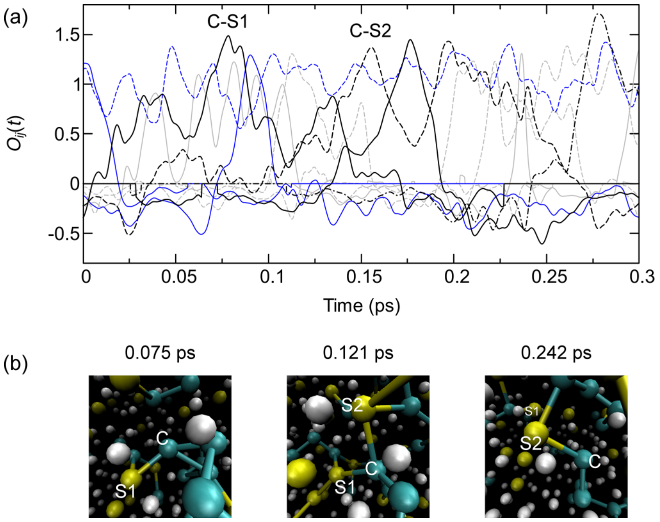

FIG. 3. (a) Time evolution of the overlap populations $O_{ij}(t)$ at 4000 K and 310 GPa. The black, blue, and gray curves are the bond-overlap populations $O_{\mathrm{CS}}(t)$, $O_{\mathrm{CC}}(t)$, and $O_{\mathrm{CH}}(t)$, respectively. (b) Atomic configurations around the selected carbon at $t = 0.075$, 0.121, and 0.242 ps. The white, cyan, and yellow spheres correspond to H, C, and S atoms, respectively. The most important atoms are labeled.

Figures 5(a) and 5(b) show the lifetimes of C–H, C–C, and C–S, as functions of pressure along the 4000 K isotherm. To compare the $\tau_{\mathrm{C\text{–}H}}$ and $\tau_{\mathrm{C\text{–}C}}$ results between the mixed and CH_4 systems, we calculated the deviation $(\tau_\alpha^{\mathrm{mixture}} - \tau_\alpha^{\mathrm{CH_4}})/\tau_\alpha^{\mathrm{CH_4}}$. The deviations for $\tau_{\mathrm{C\text{–}H}}$ and $\tau_{\mathrm{C\text{–}C}}$ are shown in Figs. 5(b) and 5(d), respectively. The deviations in $\tau_{\mathrm{C\text{–}H}}$ initially exhibit negative values and then approach zero as pressure increases. These negative deviations can be attributed to the enhanced molecular dissociation of CH_4 caused by the corrosive effect of H_2S as we explained in Sec. III C.

The enhanced molecular dissociation of CH_4 has been confirmed both experimentally and theoretically in CH_4–H_2O mixed systems [34,36], suggesting that H_2S exerts an effect similar to that of H_2O on hydrocarbons. As shown in Fig. S3 [52], the CH_4–H_2S mixed system results indicate that CH_4 molecules dissociate and C–C bonds are formed at the lowest temperature and pressure of 3000 K and 46.2 GPa. However, for CH_4–H_2O mixed systems, no C–C bonds are formed under similar conditions of 3000 K and 50 GPa [34]. This discrepancy in the structural properties of carbon suggests that H_2S is more effective than water in dissociating CH_4, thereby promoting the formation of longer hydrocarbons. Furthermore, these conditions occur in the upper mantle region of Uranus and Neptune [3], suggesting that H_2S may promote the molecular dissociation of CH_4 under planetary interior conditions.

As shown in Figs. 5(c) and 5(d), the $\tau_{\mathrm{C\text{–}C}}$ value in the mixed system deviates by 15 to −16% compared with the CH_4 system. Below approximately 200 GPa along the 4000 K isotherm, the positive deviation can be attributed to enhanced CH_4 molecular dissociation, which increases the stability of longer hydrocarbons. Figure 6 shows the deviations of $\tau_{\mathrm{C\text{–}C}}$ from 4000 K and 40 GPa to 10 000 K and 700 GPa, along with the melting line of diamond [69] and planetary interior models for Uranus and Neptune [70]. Positive deviations

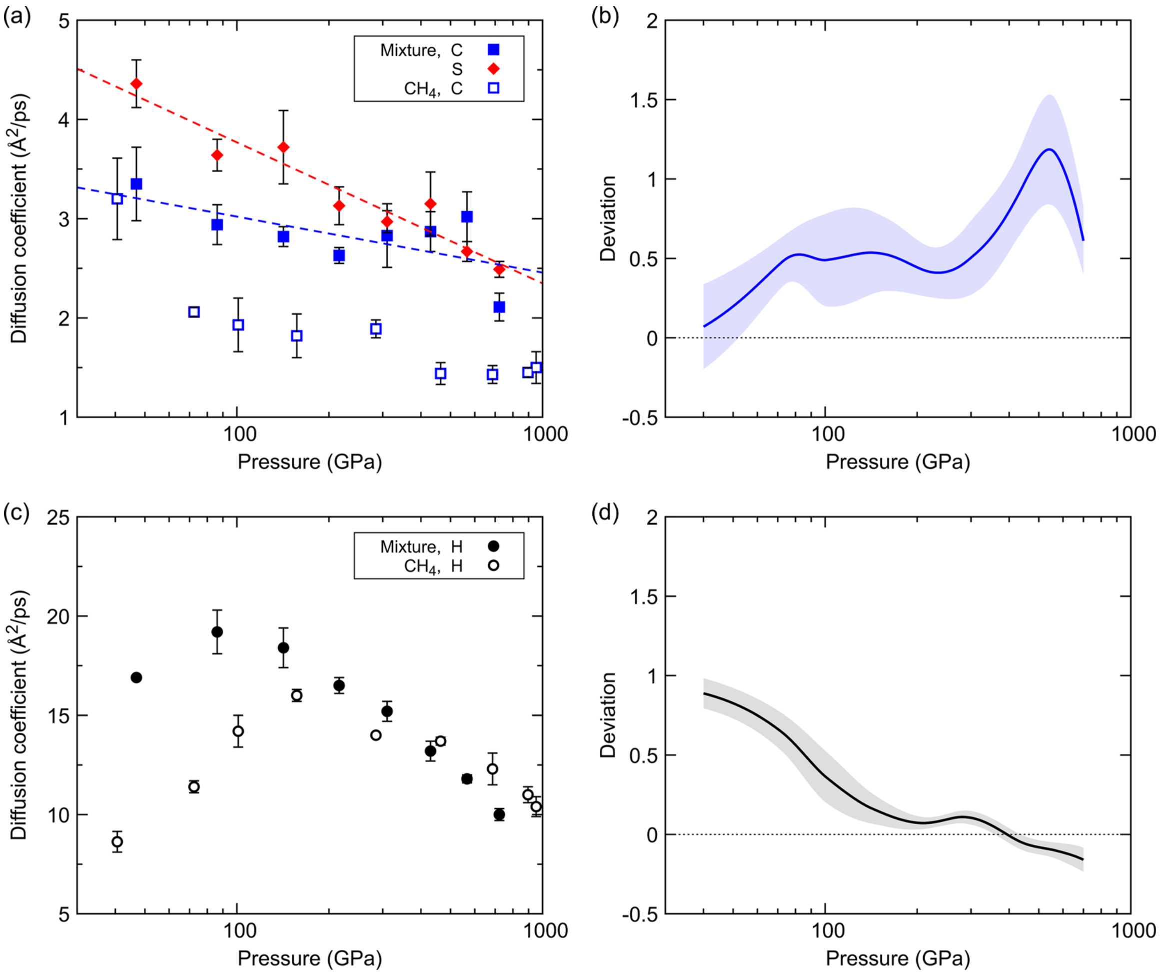

FIG. 4. (a) Carbon (D_C) and sulfur (D_S) diffusion coefficients along the 4000 K isotherm. The dashed blue and red lines give linear fits for the D_C and D_S, respectively. (b) Deviation of D_C in the mixture system relative to the CH_4 system. (c) Hydrogen diffusion coefficient along the 4000 K isotherm. (d) Deviation of D_H in the mixture system relative to the CH_4 system.

can be observed below approximately 6000 K and 150 GPa. Furthermore, the average C–C coordination at 4000 K and 86 GPa, calculated by integrating $g_{CC}(r)$ up to its first minimum, is only 1.1. However, the finite-time durations and system sizes of AIMD simulations cannot completely rule out the possibility of carbon aggregation and diamond formation, given the temperature and pressure conditions where diamond formation is observed by shock-compression experiments [2,14,19].

Above 200 GPa along the 4000 K isotherm, the $\tau_{C\text{–}C}$ values exhibit negative deviations, indicating that the C–C bonds become unstable owing to the strong correlation between carbon and sulfur atoms. The regions above 200 GPa along the 4000 K isotherm correspond to the conditions under which diamond formation from hydrocarbons occurs [18]. Therefore, the highly diffusive carbon atoms, as discussed in Sec. III C, along with the destabilization of the C–C bonds, suggest that carbon aggregation is hindered. Consequently, this slows the liquid–liquid phase separation [18] and potentially prevents diamond formation. Thus, H_2S has an adverse effect on carbon aggregation above 200 GPa along the 4000 K isotherm. As the temperature increases, the influence of H_2S on $\tau_{C\text{–}C}$ decreases.

Based on our microscopic evidence, it may be premature to conclude that complete phase separation and diamond precipitation [19] occur in the mixed system. To further investigate whether separation of carbon and sulfur occurs in the mixed system, a thermodynamic approach should be employed. Shock-compression experiments on precompressed materials [28] could achieve the conditions we examined, which involve several thousand kelvin and a few hundred GPa [71]. We propose conducting these experiments on a mixture of CH_4 and H_2S to verify our predictions.

IV. SUMMARY AND CONCLUSION

We investigated the $CH_4{-}H_2S$ mixed system at temperatures ranging from 3000 to 10 000 K and pressures up to 1500 GPa using AIMD simulations coupled with Mulliken population analysis [50,51]. To examine the structural and chemical bonding properties of the mixed system, we calculated pair distribution functions and bond-overlap populations. Our results indicate that covalent C–C and C–S bonds formed following molecular dissociation, and that hydrogen atoms could be separated from the heavier C and S atoms.

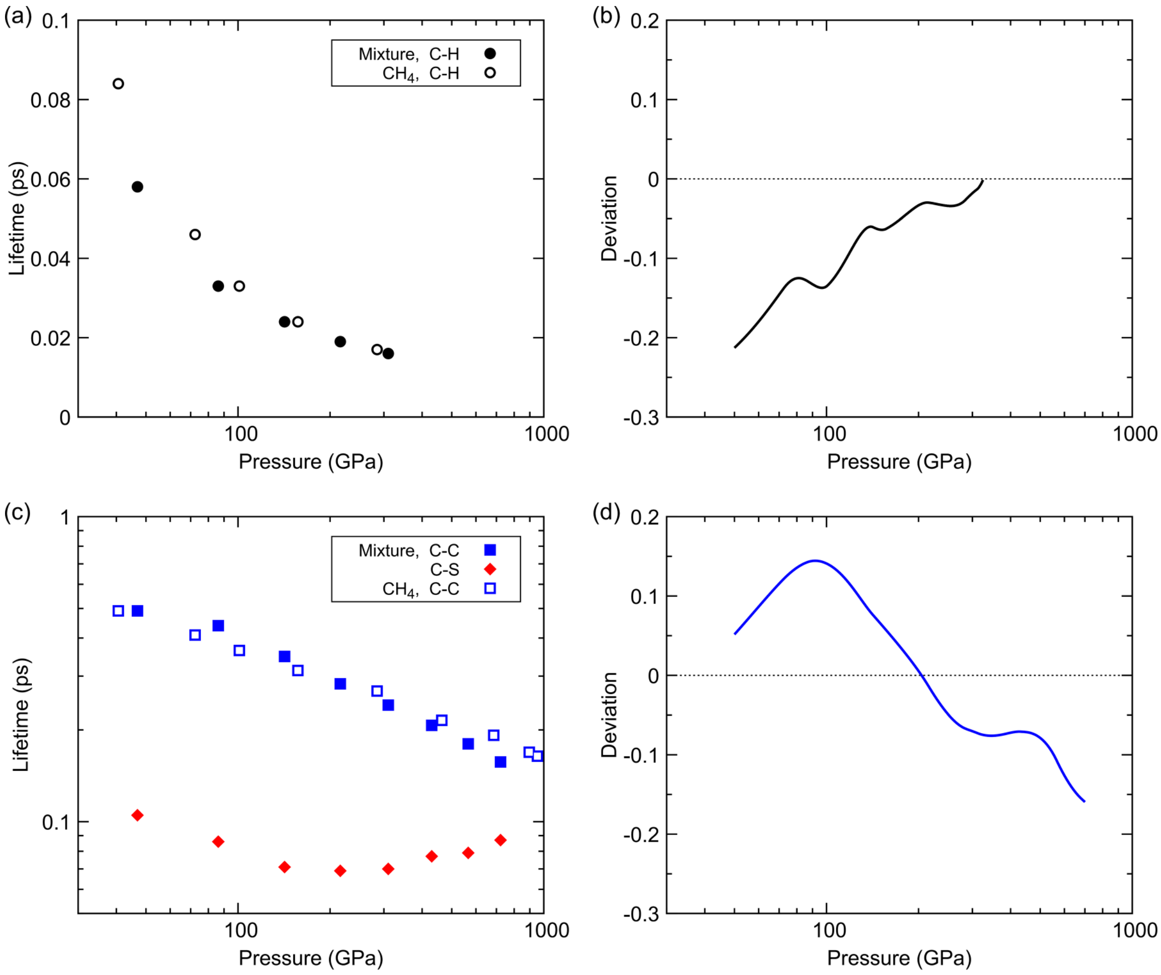

FIG. 5. Bond lifetimes of (a) H–C and (c) C–C and C–S along the 4000 K isotherm. (b) $\tau_{C–H}$ and (d) $\tau_{C–C}$ in the mixture relative to the CH_4 system, respectively.

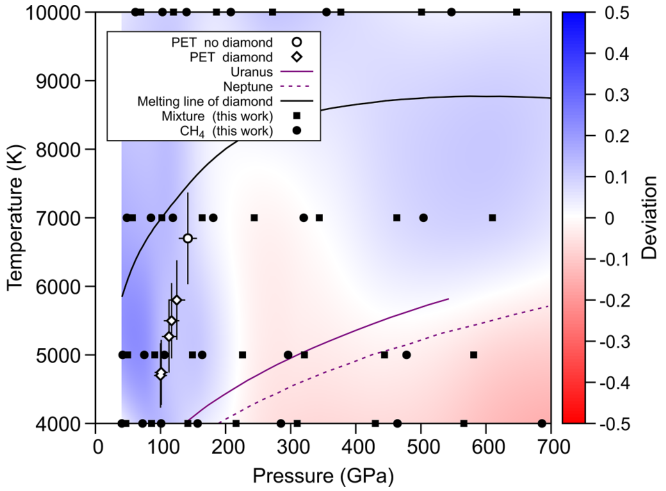

FIG. 6. Deviation between the lifetime of the C–C bonds in the mixture and CH_4 systems from 4000 K and 40 GPa to 10 000 K and 700 GPa. The data obtained from the mixture and CH_4 systems in this study are shown as filled black squares and circles, respectively. The Hugoniot of polyethylene terephthalate [2], melting line of diamond [69], and predicted interior conditions of Uranus and Neptune [70] are presented.

These covalent bonds persisted even at 722 GPa along the 4000 K isotherm.

Furthermore, our findings suggest that strong C–S bonds affect the carbon aggregation processes. Compared with the CH_4 system, hydrogen atoms in the mixed system exhibited increased diffusivity and $\tau_{C–H}$ decreased below 200 GPa. This behavior suggests that H_2S promotes the molecular dissociation of CH_4, similar to observations in a CH_4-H_2O mixed system [34,36], which possibly enhances the formation of longer hydrocarbons and diamonds. In addition, the carbon atoms in the mixture were more diffusive, and $\tau_{C–C}$ decreased above 200 GPa, indicating that H_2S potentially hinders carbon aggregation owing to the strong correlation between the carbon and sulfur atoms.

Our findings elucidate the microscopic behavior of CH_4-H_2S systems and the influence of H_2S on carbon aggregation under extreme conditions relevant to the icy giants. The 1:1 ratio of the CH_4-H_2S system considered in this study differs significantly from the solar abundance, which has a 20:1 ratio [48]. Therefore, the calculated deviations in the diffusion coefficients and bond lifetimes between the mixture and CH_4 systems should be considered upper bounds.

ACKNOWLEDGMENTS

The simulations were performed using the computer facilities at the Research Institute for Information Technology, Kyushu University, and the D3 Center, Osaka University. This work was supported by the MEXT Quantum Leap Flagship Program (Grant No. JPMXS0118067246), the Japan Society for the Promotion of Science KAKENHI (Grants No. 20H00139, No. 23K20038, and No. 23K22588), and Core-to-core program (Grant No. JPJSCCA20230003).

---

[1] S. X. Hu, T. R. Boehly, and L. A. Collins, Properties of warm dense polystyrene plasmas along the principal Hugoniot, Phys. Rev. E **89**, 063104 (2014).

[2] Z. He, M. Rödel, J. Lütgert, A. Bergermann, M. Bethkenhagen, D. Chekrygina, T. E. Cowan, A. Descamps, M. French, E. Galtier, A. E. Gleason, G. D. Glenn, S. H. Glenzer, Y. Inubushi, N. J. Hartley, J.-A. Hernandez, B. Heuser, O. S. Humphries, N. Kamimura, K. Katagiri *et al.*, Diamond formation kinetics in shock-compressed C–H–O samples recorded by small-angle x-ray scattering and x-ray diffraction, Sci. Adv. **8**, eabo0617 (2022).

[3] W. B. Hubbard, Interiors of the giant planets, Science **214**, 145 (1981).

[4] M. Ross, The ice layer in Uranus and Neptune–Diamond in the sky? Nature (London) **292**, 435 (1981).

[5] W. B. Hubbard, W. J. Nellis, A. C. Mitchell, N. C. Holmes, S. S. Limaye, and P. C. McCandless, Interior structure of Neptune: Comparison with Uranus, Science **253**, 648 (1991).

[6] W. J. Borucki, D. G. Koch, G. Basri, N. Batalha, T. M. Brown, S. T. Bryson, D. Caldwell, J. Christensen-Dalsgaard, W. D. Cochran, E. DeVore, E. W. Dunham, T. N. Gautier, III, J. C. Geary, R. Gilliland, A. Gould, S. B. Howell, J. M. Jenkins, D. W. Latham, J. J. Lissauer, G. W. Marcy *et al.*, Characteristics of planetary candidates observed by *Kepler*. II. Analysis of the first four months of data, Astrophys. J. **736**, 19 (2011).

[7] D. S. Spiegel, J. J. Fortney, and C. Sotin, Structure of exoplanets, Proc. Natl. Acad. Sci. USA **111**, 12622 (2014).

[8] R. Helled, M. Podolak, and E. Vos, Methane planets and their mass–radius relation, Astrophys. J. Lett. **805**, L11 (2015).

[9] F. Ancilotto, G. L. Chiarotti, S. Scandolo, and E. Tosatti, Dissociation of methane into hydrocarbons at extreme (Planetary) pressure and temperature, Science **275**, 1288 (1997).

[10] L. R. Benedetti, J. H. Nguyen, W. A. Caldwell, H. Liu, M. Kruger, and R. Jeanloz, Dissociation of CH_4 at high pressures and temperatures: Diamond formation in giant planet interiors? Science **286**, 100 (1999).

[11] H. Hirai, K. Konagai, T. Kawamura, Y. Yamamoto, and T. Yagi, Polymerization and diamond formation from melting methane and their implications in ice layer of giant planets, Earth Planet. Inter. **174**, 242 (2009).

[12] G. Gao, A. R. Oganov, Y. Ma, H. Wang, P. Li, Y. Li, T. Iitaka, and G. Zou, Dissociation of methane under high pressure, J. Chem. Phys. **133**, 144508 (2010).

[13] S. S. Lobanov, P.-N. Chen, X.-J. Chen, C.-S. Zha, K. D. Litasov, H.-K. Mao, and A. F. Goncharov, Carbon precipitation from heavy hydrocarbon fluid in deep planetary interiors, Nat. Commun. **4**, 2446 (2013).

[14] D. Kraus, J. Vorberger, A. Pak, N. J. Hartley, L. B. Fletcher, S. Frydrych, E. Galtier, E. J. Gamboa, D. O. Gericke, S. H. Glenzer, E. Granados, M. J. MacDonald, A. J. MacKinnon, E. E. McBride, I. Nam, P. Neumayer, M. Roth, A. M. Saunders, A. K. Schuster, P. Sun, T. van Driel, T. Döppner, and R. W. Falcone, Formation of diamonds in laser-compressed hydrocarbons at planetary interior conditions, Nat. Astro. **1**, 606 (2017).

[15] A. S. Naumova, S. V. Lepeshkin, and A. R. Oganov, Hydrocarbons under pressure: Phase diagrams and surprising new compounds in the C–H system, J. Phys. Chem. C **123**, 20497 (2019).

[16] E. B. Watkins, R. C. Huber, C. M. Childs, A. Salamat, J. S. Pigott, P. Chow, Y. Xiao, and J. D. Coe, Diamond and methane formation from the chemical decomposition of polyethylene at high pressures and temperatures, Sci. Rep. **12**, 631 (2022).

[17] A. Semerikova, A. D. Chanyshev, K. Glazyrin, A. Pakhomova, A. Kurnosov, K. Litasov, L. Dubrovinsky, T. Fedotenko, E. Koemets, and S. Rashchenko, Does it "Rain" diamonds on Neptune and Uranus? ACS Earth Space Chem. **7**, 582 (2023).

[18] B. Cheng, S. Hamel, and M. Bethkenhagen, Thermodynamics of diamond formation from hydrocarbon mixtures in planets, Nat. Commun. **14**, 1104 (2023).

[19] D. Kraus, J. Vorberger, N. J. Hartley, J. Lütgert, M. Rödel, D. Chekrygina, T. Döppner, T. van Driel, R. W. Falcone, L. B. Fletcher, S. Frydrych, E. Galtier, D. O. Gericke, S. H. Glenzer, E. Granados, Y. Inubushi, N. Kamimura, K. Katagiri, M. J. MacDonald, A. J. MacKinnon *et al.*, Indirect evidence for elemental hydrogen in laser-compressed hydrocarbons, Phys. Rev. Res. **5**, L022023 (2023).

[20] D. Murayama, S. Ohmura, K. Ryosuke, and N. Ozaki, Chemical bonding properties of liquid methane under high-density conditions, J. Appl. Phys. **134**, 095902 (2023).

[21] M. Frost, R. S. McWilliams, E. Bykova, M. Bykov, R. J. Husband, L. M. Andriambariarijaona, S. Khandarkhaeva, B. Massani, K. Appel, C. Baehtz, O. B. Ball, V. Cerantola, S. Chariton, J. Choi, H. Cynn, M. J. Duff, A. Dwivedi, E. Edmund, G. Fiquet, H. Graafsma *et al.*, Nat. Astron. **8**, 174 (2024).

[22] B. Heuser, A. Bergermann, M. G. Stevenson, D. Ranjan, Z. He, J. Lütgert, S. Schumacher, M. Bethkenhagen, A. Descamps, E. Galtier, A. E. Gleason, D. Khaghani, G. D. Glenn, E. F. Cunningham, S. H. Glenzer, N. J. Hartley, J. A. Hernandez, O. S. Humphries, K. Katagiri, H. J. Lee *et al.*, Release dynamics of nanodiamonds created by laser-driven shock compression of polyethylene terephthalate, Sci. Rep. **14**, 12239 (2024).

[23] B. L. Sherman, H. F. Wilson, D. Weeraratne, and B. Militzer, *Ab initio* simulations of hot dense methane during shock experiments, Phys. Rev. B **86**, 224113 (2012).

[24] H. B. Radousky, A. C. Mitchell, and W. J. Nellis, Shock temperature measurements of planetary ices: NH_3, CH_4, and "synthetic Uranus", J. Chem. Phys. **93**, 8235 (1990).

[25] W. J. Nellis, F. H. Ree, M. van Thiel, and A. C. Mitchell, Shock compression of liquid carbon monoxide and methane to 90 GPa (900 kbar), J. Chem. Phys. **75**, 3055 (1981).

[26] W. J. Nellis, D. C. Hamilton, and A. C. Mitchell, Electrical conductivities of methane, benzene, and polybutene shock

compressed to 60 GPa (600 kbar), J. Chem. Phys. **115**, 1015 (2001).

[27] D. Li, P. Zhang, and J. Yan, Quantum molecular dynamics simulations for the nonmetal-metal transition in shocked methane, Phys. Rev. B **84**, 184204 (2011).

[28] G. Tabak, J. R. Rygg, M. Millot, Y.-J. Kim, S. Hamel, P. M. Celliers, D. E. Fratanduono, S. Ali, D. Erskine, T. R. Boehly, T.-A. Suer, N. Dasenbrock-Gammon, R. Dias, S. Zhang, S. X. Hu, L. E. Hansen, B. J. Henderson, M. Zaghoo, T. Ogawa, D. Murayama *et al.*, Evidence for dissociation in shock-compressed methane, Phys. Rev. B **109**, 064102 (2024).

[29] A. K. Schuster, N. J. Hartley, J. Vorberger, T. Döppner, T. van Driel, R. W. Falcone, L. B. Fletcher, S. Frydrych, E. Galtier, E. J. Gamboa, D. O. Gericke, S. H. Glenzer, E. Granados, M. J. MacDonald, A. J. MacKinnon, E. E. McBride, I. Nam, P. Neumayer, A. Pak, I. Prencipe *et al.*, Measurement of diamond nucleation rates from hydrocarbons at conditions comparable to the interiors of icy giant planets, Phys. Rev. B **101**, 054301 (2020).

[30] M. S. Somayazulu, L. W. Finger, R. J. Hemley, and H. K. Mao, High-pressure compounds in methane-hydrogen mixtures, Science **271**, 1400 (1996).

[31] U. Ranieri, L. J. Conway, M.-E. Donnelly, H. Hu, M. Wang, P. Dalladay-Simpson, M. Peña-Alvarez, E. Gregoryanz, A. Hermann, and R. T. Howie, Formation and stability of dense methane-hydrogen compounds, Phys. Rev. Lett. **128**, 215702 (2022).

[32] A. J. Roy, A. Bergermann, M. Bethkenhagen, and R. Redmer, Mixture of hydrogen and methane under planetary interior conditions, Phys. Chem. Chem. Phys. **26**, 14374 (2024).

[33] H. Gao, C. Liu, A. Hermann, R. J. Needs, C. J. Pickard, H.-T. Wang, D. Xing, and J. Sun, Coexistence of plastic and partially diffusive phases in a helium-methane compound, Natl. Sci. Rev. **7**, 1540 (2020).

[34] M.-S. Lee and S. Scandolo, Mixtures of planetary ices at extreme conditions, Nat. Commun. **2**, 185 (2011).

[35] C. G. Pruteanu, G. J. Ackland, W. C. K. Poon, and J. S. Loveday, When immiscible becomes miscible–Methane in water at high pressures, Sci. Adv. **3**, e1700240 (2017).

[36] H. Kadobayashi, S. Ohnishi, H. Ohfuji, Y. Yamamoto, M. Muraoka, S. Yoshida, N. Hirao, S. Kawagushi-Imada, and H. Hirai, Diamond formation from methane hydrate under the internal conditions of giant icy planets, Sci. Rep. **11**, 8165 (2021).

[37] R. Hu, Y. Li, C. Wang, Y. Hu, and M. Lv, Quantum molecular dynamics simulations of methane-water mixture at extreme conditions in Uranus and Neptune, Phys. Rev. B **107**, 174108 (2023).

[38] W. J. Nellis, N. C. Holmes, A. C. Mitchell, D. C. Hamilton, and M. Nicol, Equation of state and electrical conductivity of "synthetic Uranus," a mixture of water, ammonia, and isopropanol, at shock pressure up to 200 GPa (2 Mbar), J. Chem. Phys. **107**, 9096 (1997).

[39] R. Chau, S. Hamel, and W. J. Nellis, Chemical processes in the deep interior of Uranus, Nat. Commun. **2**, 203 (2011).

[40] E. R. Meyer, C. Ticknor, M. Bethkenhagen, S. Hamel, R. Redmer, J. D. Kress, and L. A. Collins, Bonding and structure in dense multi-component molecular mixtures, J. Chem. Phys. **143**, 164513 (2015).

[41] M. Bethkenhagen, E. R. Meyer, S. Hamel, N. Nettelmann, M. French, L. Scheibe, C. Ticknor, L. A. Collins, J. D. Kress, J. J. Fortney, and R. Redmer, Planetary ices and the linear mixing approximation, Astrophys. J. **848**, 67 (2017).

[42] M. Guarguaglini, J.-A. Hernandez, T. Okuchi, P. Barroso, A. Benuzzi-Mounaix, M. Bethkenhagen, R. Bolis, E. Brambrink, M. French, Y. Fujimoto, R. Kodama, M. Koenig, F. Lefevre, K. Miyanishi, N. Ozaki, R. Redmer, T. Sano, Y. Umeda, T. Vinci, and A. Ravasio, Laser-driven shock compression of "synthetic planetary mixtures" of water, ethanol, and ammonia, Sci. Rep. **9**, 10155 (2019).

[43] L. J. Conway, C. J. Pickard, and A. Hermann, Rules of formation of H–C–N–O compounds at high pressure and the fates of planetary ices, Proc. Nat. Acad. Sci. USA **118**, e2026360118 (2021).

[44] K. de Villa, F. G.-Cataldo, and B. Militzer, Double superionicity in icy compounds at planetary interior conditions, Nat. Commun. **14**, 7580 (2023).

[45] A. P. Drozdov, M. I. Eremets, I. A. Troyan, V. Ksenofontov, and S. I. Shylin, Conventional superconductivity at 203 kelvin at high pressures in the sulfur hydride system, Nature (London) **525**, 73 (2015).

[46] H. Shimizu, Y. Nakamichi, and S. Sasaki, Pressure-induced phase transition in solid hydrogen sulfide at 11 GPa, J. Chem. Phys. **95**, 2036 (1991).

[47] H. Shimizu and S. Sasaki, High-pressure Brillouin studies and elastic properties of single-crystal H_2S grown in a diamond cell, Science **257**, 514 (1992).

[48] M. Asplund, N. Grevesse, A. J. Sauval, and P. Scott, The chemical composition of the Sun, Annu. Rev. Astron. Astrophys. **47**, 481 (2009).

[49] P. G. J. Lrwin, D. Toledo, R. Garland, N. A. Teanby, L. N. Fletcher, G. A. Orton, and B. Bézard, Detection of hydrogen sulfide above the clouds in Uranus's atmosphere, Nat. Astron. **2**, 420 (2018).

[50] R. S. Mulliken, Electronic population analysis on LCAO–MO molecular wave functions. II. Overlap populations, bond orders, and covalent bond energies, J. Chem. Phys. **23**, 1841 (1955).

[51] F. Shimojo, A. Nakano, R. K. Kalia, and P. Vashishta, Electronic processes in fast thermite chemical reactions: A first-principles molecular dynamics study, Phys. Rev. E **77**, 066103 (2008).

[52] See Supplemental Material at http://link.aps.org/supplemental/10.1103/PhysRevB.111.024308 for computational methods, data analysis, and supplemental Figs. S1–S15 and Table SI–SIII, which includes Refs. [36,50,51].

[53] F. Shimojo, R. K. Kalia, A. Nakano, and P. Vashishta, Linear-scaling density-functional-theory calculations of electronic structure based on real-space grids: Design, analysis, and scalability test of parallel algorithms, Comput. Phys. Commun. **140**, 303 (2001).

[54] F. Shimojo, S. Fukushima, H. Kumazoe, M. Misawa, S. Ohmura, P. Rajak, K. Shimamura, L. B. Oftelie, S. Tiwari, R. K. Kalia, A. Nakano, and P. Vashishta, QXMD: An open-source program for nonadiabatic quantum molecular dynamics, SoftwareX **10**, 100307 (2019).

[55] P. E. Blöchl, Projector augmented-wave method, Phys. Rev. B **50**, 17953 (1994).

[56] G. Kresse and D. Joubert, From ultrasoft pseudopotentials to the projector augmented-wave method, Phys. Rev. B **59**, 1758 (1999).

[57] P. Hohenberg and W. Kohn, Inhomogeneous electron gas, Phys. Rev. **136**, B864 (1964).

[58] W. Kohn and L. J. Sham, Self-consistent equations including exchange and correlation effects, Phys. Rev. **140**, A1133 (1965).

[59] N. D. Mermin, Thermal properties of the inhomogeneous electron gas, Phys. Rev. **137**, A1441 (1965).

[60] J. P. Perdew, K. Burke, and M. Ernzerhof, Generalized gradient approximation made simple, Phys. Rev. Lett. **77**, 3865 (1996).

[61] G. Kresse and J. Hafner, *Ab initio* molecular-dynamics simulation of the liquid-metal-amorphous-semiconductor transition in germanium, Phys. Rev. B **49**, 14251 (1994).

[62] H. J. Monkhorst and J. D. Pack, Special points for Brillouin-zone integrations, Phys. Rev. B **13**, 5188 (1976).

[63] S. Nosé, A molecular dynamics method for simulations in the canonical ensemble, Mol. Phys. **52**, 255 (1984).

[64] W. G. Hoover, Canonical dynamics: Equilibrium phase-space distributions, Phys. Rev. A **31**, 1695 (1985).

[65] M. Tuckerman, B. J. Berne, and G. J. Martyna, Reversible multiple time scale molecular dynamics, J. Chem. Phys. **97**, 1990 (1992).

[66] X. Bokhimi, Atomic and electronic properties of a 155 H_2S custer under pressure, ACS Omega **4**, 10524 (2019).

[67] L. Liu, Y. Kono, C. K. Benson, W. Yang, Y. Bi, and G. Shen, Chain breakage in liquid sulfur at high pressures and high temperatures, Phys. Rev. B **89**, 174201 (2014).

[68] S. Ohmura and F. Shimojo, Structural change in liquid sulphur from chain polymeric liquid to atomic simple liquid under high pressure, J. Phys.: Condens. Matter **31**, 215101 (2019).

[69] X. Wang, S. Scandolo, and R. Car, Carbon phase diagram from *Ab Initio* molecular dynamics, Phys. Rev. Lett. **95**, 185701 (2005).

[70] R. Redmer, T. R. Mattsson, N. Nettelmann, and M. French, The phase diagram of water and the magnetic fields of Uranus and Neptune, Icarus **211**, 798 (2011).

[71] M. Millot, F. Coppari, J. R. Rygg, A. C. Barrios, S. Hamel, D. C. Swift, and J. H. Eggert, Nanosecond x-ray diffraction of shock-compressed superionic water ice, Nature (London) **569**, 251 (2019).